Available online at www.sciencedirect.com
SCIENCE DIRECT®
Journal of Magnetic Resonance 173 (2005) 10–22
JMR Journal of Magnetic Resonance
www.elsevier.com/locate/jmr

Computer simulation studies of the effects of dynamic shimming on susceptibility artifacts in EPI at high field

Yansong Zhao[a,*], Adam W. Anderson[b], John C. Gore[b]

[a] Department of Electrical Engineering, Yale University, New Haven, CT 06520, USA
[b] Institute of Imaging Science, Vanderbilt University, Nashville, TN 37235, USA

Received 29 April 2004; revised 1 November 2004
Available online 8 December 2004

Abstract

Dynamic shimming in multi-slice imaging aims to achieve optimal magnetic field homogeneity by updating the shim coil currents for each slice in real time. Dynamic shimming may reduce the signal loss and geometric distortion caused by magnetic susceptibility variations between tissues and is likely to be valuable for fast T_2^*-sensitive imaging techniques like EPI. A computer simulation of dynamic shimming using real image data has been developed to demonstrate the effectiveness of higher order dynamic shimming for echo planar imaging at high magnetic field, and to investigate the potential benefits of different orders of shim coil. Geometric distortions and signal intensities for different degrees of dynamic shimming were simulated and the results are compared with the images obtained with a conventional shimming technique. These results demonstrate the effectiveness, necessity and difficulty of high order dynamic shimming.

Keywords: Shimming; Magnetic field homogeneity; Susceptibility artifacts; Echo planar imaging; High field

1. Introduction

In magnetic resonance imaging, magnetic susceptibility variations within tissues cause distortions in the magnetic field. Such field fluctuations, which occur primarily at the interfaces of air, tissue, and bone, where the susceptibility changes rapidly over short distances, lead to two types of artifact in reconstructed T_2^*-weighted MR images, geometric distortion and signal losses [1]. These two artifacts become more severe in widely used fast gradient echo imaging techniques, such as gradient echo EPI, which are extremely sensitive to field inhomogeneities. In functional MRI, the processed functional images are usually overlaid onto higher resolution anatomical images to show the location of activated brain regions. Geometric distortions within the images lead to errors in the localization of activity, while signal losses may create signal voids that then cannot be studied. Many regions of brain that might be of interest for functional studies, such as the frontal lobes and the temporal lobes, are impossible or difficult to examine with such gradient echo techniques. Although the BOLD effect increases with magnetic field strength, susceptibility artifacts also are more severe at higher field. The development of methods to reduce the effects of susceptibility variations is an important goal for the further exploitation of high field imaging.

Several methods have been proposed for reducing susceptibility artifacts. Such methods include automatic shimming [2–9], z-shimming [10–13], the use of tailored RF (TRF) pulses [14–16] and various post-processing methods [17–20]. z-shimming and TRF recover signal losses by correcting the through-plane intravoxel dephasing, while most post-processing methods are designed to correct geometric distortions caused mostly

* Corresponding author. Present address: Institute of Imaging Science, CCC 1121 MCN, Nashville, TN 37232-2675, USA. Fax: +1 615 332 0734.
E-mail address: yansong.zhao@yale.edu (Y. Zhao).

1090-7807/$ - see front matter © 2004 Elsevier Inc. All rights reserved.
doi:10.1016/j.jmr.2004.11.009

by in-plane phase errors. Automatic shimming aims to achieve optimal field homogeneity and reduce both geometric distortion and signal losses. Conventional "global" shimming techniques [2–4] optimize the magnetic field over the entire volume imaged, but with this approach, localized field inhomogeneities caused by susceptibility effects, which are often concentrated within a specific area and weight only a small part of the whole volume, cannot be effectively minimized. Blamire et al. [6] and Morrell et al. [7] proposed a "dynamic" shimming method that optimizes the field homogeneity locally by updating shim currents slice by slice in real time during interleaved data acquisition. This method has been extended recently to include both first- and second-order shims [9]. Compared with global shimming methods, dynamic shimming should refine the magnetic field homogeneity more effectively, especially in the areas where susceptibility effects are strong.

On current imaging systems, the only shim coils that can usually be updated in real time are the three first order linear gradients in Z, X, and Y. Higher order shim coils are usually not actively shielded and potentially may cause severe eddy currents if updated dynamically. In earlier studies only Z, X, Y, and $Z0$ were adjusted in dynamically shimming whole brain [7]. However, some regions in brain, such as the temporal lobes and the anterior frontal lobes demand higher order shims to remove the effects of local variations. In general however, the specific practical advantages of adding additional terms have not been systematically investigated. The addition of dynamic shims of 2nd, 3rd or even higher orders would add cost and complexity to MRI systems, and dynamic changes in shim currents may require creation of shielded shim coils. We therefore developed a computer simulation to investigate how higher order dynamic shimming may benefit echo planar imaging, chemical shift imaging, and how it may affect MRI hardware design. We have calculated and compared the field distributions within the head for different orders of dynamic shimming and for global shimming, together with the signal intensity and geometric distortions for a typical echo planar imaging experiment, at different field strengths. This simulation uses a new method for the shim calculations. The field magnitudes in any three adjacent slices were used in a least-squares multi-linear regression to estimate the shim settings for the middle slice. This results in greater through-plane homogeneity in the resultant field distribution, and thus less signal loss in the final images.

2. Methods

Computer simulations were written in Matlab (The MathWorks Natick, MA) and performed on a PC platform with 3 GHz Pentium4 processor and 1 GB memory. The first step for automatic shimming was mapping the field variation in the volume of interest using MR imaging. Then shim currents are calculated by decomposing the measured field into orthogonal components. Details of the field mapping and shim current calculation are described below, as well as the methods used to calculate signal intensity and geometric distortion.

2.1. Field mapping

Two sets of static magnetic field maps within a human head were acquired using a 1.5 T MRI scanner (GE Medical Systems, Milwaukee WI). The field maps were calculated from the phase difference of two gradient echo images obtained at different echo time with multi-slice 2D gradient echo imaging and 3D gradient echo imaging [3]. The unwrapped phases of the complex images were subtracted and then divided by the difference in echo times to yield a frequency map. Data were collected as $256 \times 256 \times 15$ and $256 \times 256 \times 60$ coronal images, respectively. Field of View (FOV) was 24 cm with 5 mm slice thickness and 12 mm interval for 2D data and $30 \times 30 \times 18$ cm for 3D data. Geometric distortions in these images, which were obtained at high bandwidth, were neglected. The field maps were then scaled by 4/1.5 and 7/1.5 to simulate the field maps at 4.0 and 7.0 T scanning.

2.2. Shimming

The static magnetic field in MRI can be expanded using spherical harmonics as orthogonal base functions, and each term is then represented by a shim coil correction [21]. Shimming is the process of adjusting each coil to cancel the unwanted harmonics. A limited number of shim fields are available on any system, each of which is produced by a coil and associated with one particular spatial field distribution. Least-squares multiple linear regression was used to decompose the measured field maps in the brain into component spherical harmonics. A "brain mask" was generated through segmentation and was applied onto the field maps before decomposition so that only voxels inside the brain were used to weight the fitting.

As many as 18 coils are often provided for shimming: zero order: $Z0$ (center frequency); first order: Z, X, Y; second order: $Z2$, ZX, ZY, $X2-Y2$, XY; third order: $Z3$, $Z2X$, $Z2Y$, $Z(X2–Y2)$, ZXY, $X3$, $Y3$; fourth and fifth order: $Z4$, $Z5$. In our simulation, all these 18 shim terms were optimized to show the best homogeneity that dynamic shimming can achieve. Dynamic shimming with only first and second order terms were also simulated to evaluate how effectively a more limited set of coils could perform in practice.

The difference between global shimming and dynamic shimming is that the optimal shim terms for any slice or region may not be the same for all slices. Global shimming aims to achieve optimal shimming over the whole volume. The field magnitudes at all points in the volume of interest (VOI) are used to weight the linear regression to get one set of coefficients for the whole volume. This set of shim currents is then constant during scanning. Dynamic shimming, on the other hand, aims to achieve optimal shimming over each single slice. Only the field magnitudes in the particular slice(s) to be imaged are used in the linear regression to obtain a set of coefficients for this slice. Shim currents are then updated before scanning the next slice. In this way, local field inhomogeneities, which may not be dominant over the entire VOI, can be removed by dynamic shimming.

In this study, the field magnitudes in sets of three adjacent slices were used to calculate the coefficients for the middle slices (for the first and last slices, only two slices are involved in the calculation). This allows us to calculate not only the in-plane homogeneity but also to accurately estimate through-plane effects. In most MR imaging experiments, the slice thickness tends to be larger than the resolution within the plane, so this relatively large slice thickness tends to disperse the spin phases during the echo time and causes most of the signal loss. A more homogeneous through-plane magnetic field will recover more signal loss.

The homogeneity achieved was compared using the standard deviation and the mean value of the frequency deviations over each field map. The coefficients obtained from the linear regression are shim current gradients in Hz/cm^n, where n is the order of shim harmonics. From the changes of these gradients between slices, eddy currents can be estimated qualitatively.

2.3. Simulation of geometric distortion

Susceptibility variations produce both signal losses and geometric distortion in EPI. The effectiveness of higher order dynamic shimming on these susceptibility artifacts may be demonstrated by comparing the signal intensities and pixel shifts obtained in a typical echo-planar imaging experiment after dynamic shimming and after conventional global shimming. We study these two artifacts in the simulation separately.

The most perceptible artifact caused by in-plane field inhomogeneities is geometric distortion. Assuming an infinitely thin slice and neglecting T_2 effects, the received signal in the present of a magnetic field inhomogeneity $\Delta B(x,y)$ can be expressed as:

$$S(k_x,k_y)=\int\int \rho(x,y)\mathrm{e}^{-\mathrm{i}(k_x x+k_y y)}\mathrm{e}^{-\mathrm{i}\gamma\Delta B(x,y)t}\,\mathrm{d}x\,\mathrm{d}y, \tag{1}$$

in which $\rho(x,y)$ is the spin density of the voxel, γ is the gyro-magnetic ratio and

$$k_x(t)=m\Delta k_x=\gamma\int_0^t G_x(t')\,\mathrm{d}t',\quad -N_x/2\leqslant m<N_x/2,$$

$$k_y(t)=n\Delta k_y=\gamma\int_0^t G_y(t')\,\mathrm{d}t',\quad -N_y/2\leqslant n<N_y/2,$$

where G_x and G_y are the gradient strengths along the readout and phase encoding directions, respectively. t is the time at nth k_y line and mth sample point (t starts at the center of 90° RF pulse):

$$t=T_{\mathrm{E}}+nT\pm m\Delta t, \tag{2}$$

T_{E} is the echo time. T is the time interval between adjacent k_y lines and Δt is the sampling "dwell" time (the time interval between the acquisition of individual data points). N_x and N_y are the matrix size for the readout and phase encoding directions, respectively. $\Delta k_x(\Delta k_y)$ represent gradient area increments in the readout (phase encoding) directions.

The received signal of a gradient echo EPI is:

$$\begin{aligned}S(k_x,k_y)&=\int\int \rho(x,y)\exp\{-\mathrm{i}(m\Delta k_x x+n\Delta k_y y)\}\\&\quad\times\exp\{-\mathrm{i}\gamma\Delta B(x,y)(nT\pm m\Delta t+T_{\mathrm{E}})\}\,\mathrm{d}x\,\mathrm{d}y\\&=\int\int[\rho(x,y)\exp\{-\mathrm{i}\gamma\Delta B(x,y)T_{\mathrm{E}}\}]\\&\quad\times\exp\{-\mathrm{i}k_x(x\pm\gamma\Delta B(x,y)\Delta t/\Delta k_x)\}\\&\quad\times\exp\{-\mathrm{i}k_y(y+\gamma\Delta B(x,y)T/\Delta k_y)\}\,\mathrm{d}x\,\mathrm{d}y.\end{aligned} \tag{3}$$

According to the Fourier shift theorem, the additional phase in k-space produced by ΔB will create a pixel shift in the reconstructed image. A pixel originally at (x,y) will be at (x_1,y_1) in the reconstructed image $\rho_1(x_1,y_1)$

$$\begin{aligned}x_1-x&=\pm\frac{\gamma\Delta B(x,y)\Delta t}{\Delta k_x},\\y_1-y&=\frac{\gamma\Delta B(x,y)T}{\Delta k_y}.\end{aligned} \tag{4}$$

For an image with pixel size of $\Delta x\times\Delta y$, $\Delta k_x=2\pi/(N_x\Delta x)$, and $\Delta k_y=2\pi/(N_y\Delta y)$. So the relative pixel shifts are:

$$\begin{aligned}\frac{x_1-x}{\Delta x}&=\pm N_x\Delta f(x,y)\Delta t,\\\frac{y_1-y}{\Delta y}&=N_y\Delta f(x,y)T,\end{aligned} \tag{5}$$

where $\Delta f(x,y)=\gamma\Delta B(x,y)/2\pi$.

Consider for example an EPI acquisition with trapezoidal read gradient waveform and triangular phase encode blips:

$$T=N_x\Delta t+2\tau_r, \tag{6}$$

where τ_r is the rise time of the switched gradient.

The relative pixel shifts become:

$$\begin{aligned}\frac{x_1-x}{\Delta x}&=\pm\frac{N_x}{\mathrm{BW}}\Delta f(x,y),\\\frac{y_1-y}{\Delta y}&=\left(2\tau_r+\frac{N_x}{\mathrm{BW}}\right)N_y\Delta f(x,y).\end{aligned} \tag{7}$$

BW is the receiver bandwidth, $\mathrm{BW}=1/\Delta t$.

Note that Eq. (7) also holds for spin echo EPI. In spin echo EPI, since a 180° pulse rephases the spins at $m = 0$, $n = 0$, the phase evolution during the echo time T_E will be zero; there will not be a phase term $\exp(-i\gamma\Delta B(x,y)T_E)$ as in the gradient echo EPI (Eq. (3)). Thus, gradient echo EPI and spin echo EPI will have identical geometric distortions, but gradient echo EPI will suffer more from signal losses.

The pixel shifts in a typical EPI experiment with 125 kHz bandwidth, 200 μs gradient rise time and 64×64 matrix were simulated. Since EPI images are geometrically distorted predominantly along the phase encoding direction, only relative pixel shifts in the phase encoding direction were calculated in the simulation. (The largest pixel shifts in the readout direction is less than 7% pixel before any shimming at 7 T in our simulation, which is barely perceptible). The root-mean-square (RMS) values of relative pixel shifts over each slice were used to quantify the gross geometric distortion of the slice.

2.4. Simulation of signal intensity

Signal losses can be more serious artifacts than geometric distortion for many applications of EPI. In a gradient echo experiment, for an individual voxel in the volume of interest, the signal induced in the NMR receiver coils is given by:

$$S = \int d^3 r \rho(r) e^{i\phi(r)}, \tag{8}$$

where $\rho(r)$ is the spin density of the voxel and $\phi(r)$ is the signal phase, which is determined by the field gradient history and field inhomogeneity.

If the voxel size is not too big, the signal phase variation within a voxel is mainly caused by the first derivative of the magnetic field. If we expand the signal phase to first order, if r_0 is the coordinate of the voxel center ($r_0 = (x_0, y_0, z_0)$) then

$$S = \int d^3 r \rho(r) e^{i\phi(r_0)} e^{i\gamma T_E \frac{\partial B}{\partial r}(r - r_0)}, \tag{9}$$

in which T_E is the echo time, B is the magnetic field distribution, $\frac{\partial B}{\partial r} = \frac{\partial B}{\partial r}|_{r=r_0}$. Assuming the spin density in the voxel is uniform $\rho(r) = \rho$, if the dimensions of the voxel are Δx, Δy, and Δz,

$$\begin{aligned} S = \rho e^{i\phi_0} & \int_{x_0-\Delta x/2}^{x_0+\Delta x/2} dx e^{i\gamma T_E \frac{\partial B}{\partial x}(x-x_0)} \\ & \times \int_{y_0-\Delta y/2}^{y_0+\Delta y/2} dy e^{i\gamma T_E \frac{\partial B}{\partial y}(y-y_0)} \\ & \times \int_{z_0-\Delta z/2}^{z_0+\Delta z/2} dz e^{i\gamma T_E \frac{\partial B}{\partial z}(z-z_0)}. \end{aligned} \tag{10}$$

The signal magnitude is:

$$\begin{aligned} |S| = \rho \Delta x \Delta y \Delta z & \operatorname{sinc}\left(\pi T_E \Delta x \frac{\partial f}{\partial x}\right) \operatorname{sinc}\left(\pi T_E \Delta y \frac{\partial f}{\partial y}\right) \\ & \times \operatorname{sinc}\left(\pi T_E \Delta z \frac{\partial f}{\partial z}\right), \end{aligned} \tag{11}$$

where $f = f(x, y, z)$ is the frequency at this voxel.

For a gradient echo EPI, besides the signal loss caused by intravoxel dephasing shown above, geometric distortion induced signal variation should also be considered. Discarding the pixel shifts along the readout direction and the slice selection direction, (x_0, y_0, z_0) is shifted to (x_0, y_1, z_0), so Eq. (10) becomes:

$$\begin{aligned} S = \rho e^{i\phi_0} \Delta x \operatorname{sinc}\left(\pi T_E \Delta x \frac{\partial f}{\partial x}\right) \Delta z \operatorname{sinc}\left(\pi T_E \Delta z \frac{\partial f}{\partial z}\right) J \\ \times \int_{y_1-\Delta y/2}^{y_1+\Delta y/2} dy' \exp\left\{ i\gamma T_E \frac{\partial B}{\partial y} \frac{dy}{dy'} (y' - y_1) \right\}, \end{aligned} \tag{12}$$

in which J is the Jacobian introduced by change of variable and can be calculated from Eq. (7)

$$J = \frac{dy}{dy_1} = \frac{1}{1 + N_y \Delta y \left(\frac{N_x}{BW} + 2\tau_r\right) \frac{\partial f}{\partial y}}. \tag{13}$$

The signal magnitude for a gradient echo EPI is then:

$$\begin{aligned} |S| = \rho \Delta x \Delta y \Delta z & \operatorname{sinc}\left(\pi T_E \Delta x \frac{\partial f}{\partial x}\right) \operatorname{sinc}\left(J \pi T_E \Delta y \frac{\partial f}{\partial y}\right) \\ & \times \operatorname{sinc}\left(\pi T_E \Delta z \frac{\partial f}{\partial z}\right) J. \end{aligned} \tag{14}$$

The Jacobian allows for a signal magnitude variation originating from geometric distortion. Since in this study, signal losses due to introvoxel dephasing and geometric distortion due to phase errors were studied separately, we used Eq. (11) instead of Eq. (14) to calculate the signal magnitude.

3. Results

The field maps of 4 coronal slices before shimming at 7 T are shown in Fig. 1. Large magnetic field variations can be seen at the brain boundaries, especially at the anterior part of the brain (Figs. 1C and D). In the posterior part of brain (Figs. 1A and B), the field distribution is dominated by linear variations throughout the whole brain area. In the anterior part of brain, higher order terms become severe and they concentrate in a small area near the air/tissue interfaces.

Fig. 2 shows the mean values and standard deviations of the field maps of the 15 2D coronal slices of the brain after global shimming and after dynamic shimming at 7 T, both using all 18 shim terms. As expected, the field distribution after dynamic shimming has a smaller mean value and smaller standard deviation at each slice. In the posterior part of the brain (the horizontal axis is in the

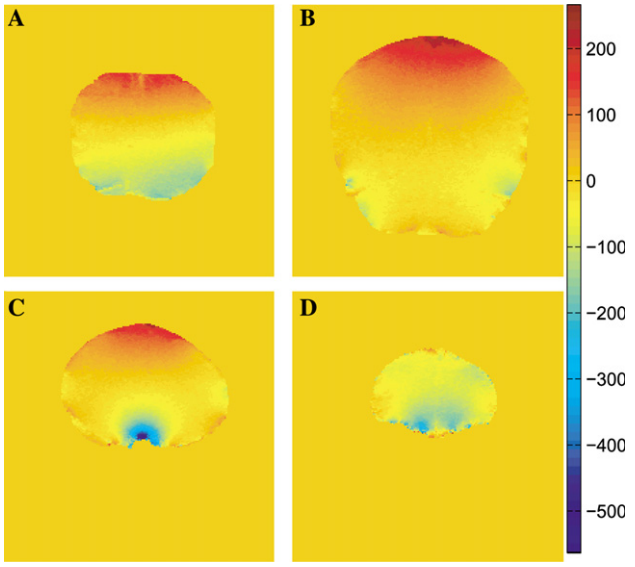

Fig. 1. Experimentally measured field maps (in Hz) of 4 coronal slices before shimming at 7 T. The slices are (A) −7.2 cm, (B) −3.6 cm, (C) 3.6 cm, and (D) 7.2 cm from isocenter.

posterior/anterior direction), the field is relatively homogeneous, but dynamic shimming gives some improvement over global shimming. As the imaging slice moves to the anterior area, where the nasal cavity and frontal sinuses cause pronounced field variations, dynamic shimming "weights" this change in calculating the shim currents and obtains a much more homogeneous field than global shimming. Fig. 3 shows the behavior of the in-plane Z-shim on its own. The dashed line represents the 3.00 mG/cm shim gradient value used in global shimming. The solid line represents the dynamically adjusted value of this shim gradient in dynamic shimming. Before slice 10 (2.4 cm away from magnet isocenter), the optimal Z shim gradient changes in the range of 1.33–3.00 mG/cm. After slice 10, a shim gradient as high as 80 mG/cm is required to optimize the local field along z (superior/inferior). Other shim gradients are list in Table 1. Similar results were found from 3D data and 4 T simulations.

Both global shimming and dynamic shimming recover signal losses, but dynamic shimming produces a higher signal magnitude than global shimming at every slice, especially in the anterior part of the brain. The relative signal intensity improvement $\Delta I = (I_d - I_g)/I_g$ is used to show the signal improvement of dynamic shimming over global shimming (see Fig. 4). I_d and I_g are the mean signal intensities over each image after dynamic shimming and after global shimming, respectively. Many slices showed noticeable intensity improvement, no slice showed degradation. Since the mean signal

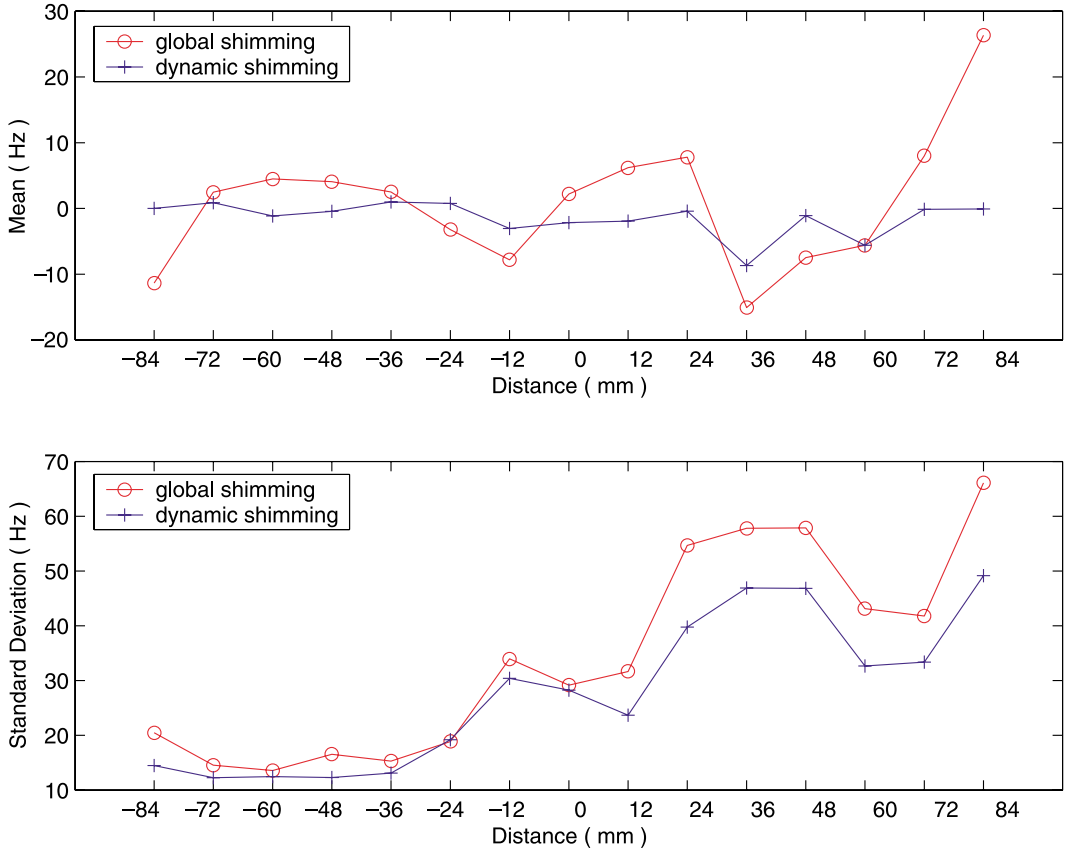

Fig. 2. Simulation comparison of the mean value and standard deviation of 15 coronal field maps after global shimming and dynamic shimming with all (18) available shim terms at 7 T.

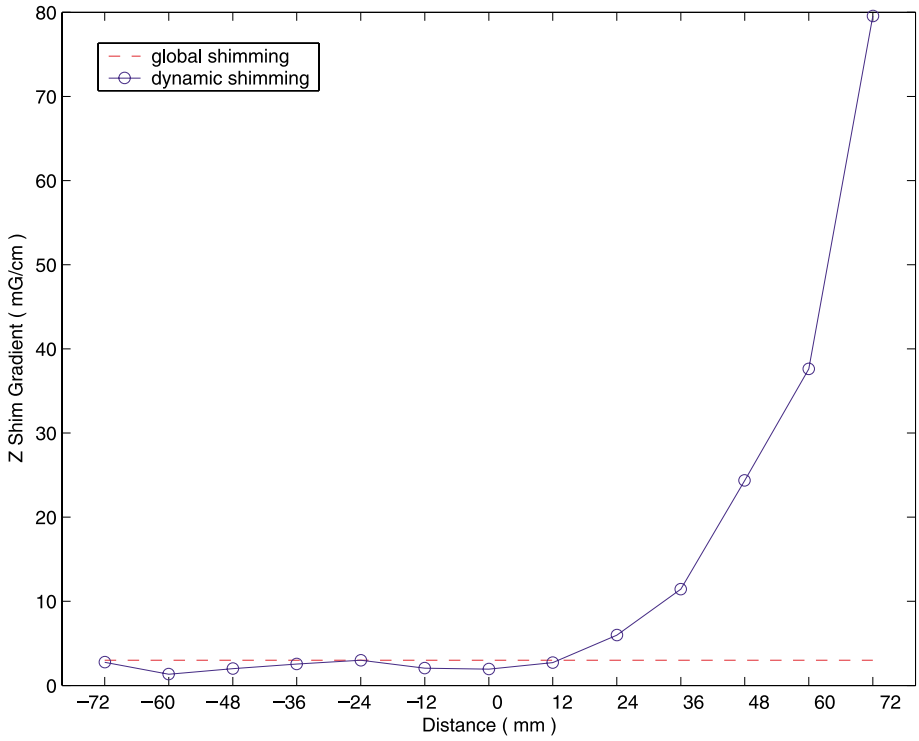

Fig. 3. Simulated Z-shim gradient change from posterior to anterior during 18 terms dynamic shimming at 7 T. Dashed line is the 3.00 mG/cm z-shim value in global shimming. z is the phase encoding direction.

Table 1
Simulated shim gradients of first 9 shim terms in global shimming and dynamic shimming at 7 T

	Shim gradients (mG/cm^n)								
	$Z0$	Z	X	Y	$Z2$	ZX	ZY	$X2$–$Y2$	XY
Global shimming:	5.75	3.00	−0.65	1.17	0.60	−0.02	0.12	0.03	0.01
Dynamic shimming (slice #/distance (mm))									
1/−84	−15.29	29.24	−2.85	7.66	−0.14	−0.39	−3.11	0.38	0.10
2/−72	32.40	2.75	−1.23	−10.67	−1.50	−0.13	−0.25	−0.26	0.02
3/−60	12.96	1.33	−1.32	−3.07	−0.41	0.01	0.21	−0.12	0.03
4/−48	6.56	2.00	−1.28	0.22	0.18	−0.01	0.22	−0.02	0.03
5/−36	5.59	2.54	−1.31	0.77	0.32	−0.01	0.18	0.01	0.03
6/−24	8.45	3.00	−1.18	−0.60	0.35	0.06	0.14	−0.07	0.02
7/−12	7.38	2.05	−0.94	−0.14	0.54	0.02	0.24	−0.02	0.01
8/0	5.26	1.94	−0.78	2.80	0.72	0.04	0.30	0.04	−0.04
9/12	6.56	2.72	−0.93	4.43	0.62	−0.02	0.27	0.00	−0.07
10/24	3.39	5.98	−0.83	2.29	0.98	−0.01	0.72	0.00	−0.06
11/36	−19.10	11.44	1.07	−8.34	2.16	0.07	1.52	0.27	0.06
12/48	−40.35	24.37	5.03	−11.16	0.92	−0.59	2.03	0.36	0.17
13/60	−108.64	37.62	3.61	−37.53	4.23	−0.22	4.08	0.90	0.10
14/72	−182.82	79.56	4.24	−51.97	3.83	−1.17	7.41	0.79	0.12
15/84	−596.80	225.39	−8.90	−182.52	11.06	−3.46	23.97	3.16	−0.57

n is the order of shim term, $n = 0$ ($Z0$), $n = 1$ (Z, X, Y), and $n = 2$ ($Z2, ZX, ZY, X2$–$Y2, XY$).

intensity over an entire image is used to show the improvement at each slice, the ability of dynamic shimming to recover signal loss at local areas is under-estimated. For instance, at slice 9, an improvement of 5.6% is shown. If we look at the 40×40 sub-area at bottom right of the brain, where susceptibility artifacts were stronger, more than 22.0% increase can be found. Intensity images and field maps of three slices before and after shimming are shown in Fig. 5. The left column shows the field maps and intensity images before shimming. The middle column and right column are field maps and intensity images after global shimming and after dynamic shimming, respectively. Slice 9 and slice 14 are from 2D coronal data. These two slices are about 1.2

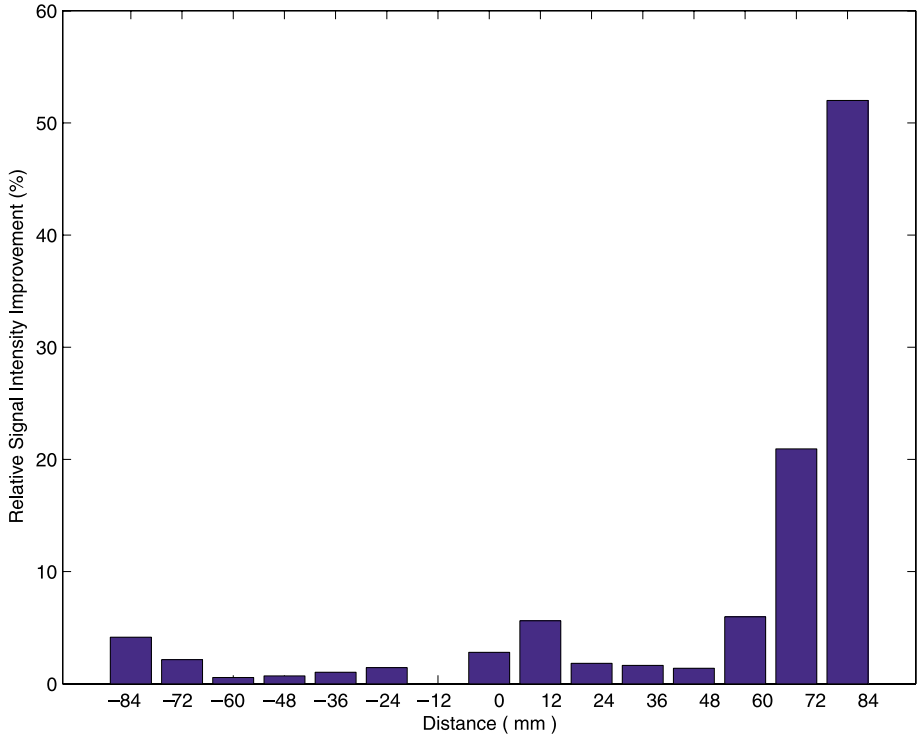

Fig. 4. Simulated relative signal intensity improvement of dynamic shimming over global at 7 T.

and 7.2 cm apart from the magnet center, respectively. Slice 27 is a transaxial slice calculated from 3D coronal data and is 1.8 cm from isocenter. Intensity improvements were observed at air/tissue interfaces in the brain after dynamic shimming. Notice that in this figure only signal intensity effects were simulated without considering geometric distortions.

RMS pixel shifts along the phase encoding direction are shown in Fig. 6A. Again, dynamic shimming corrects more geometric distortions than global shimming at each slice. For posterior slice 1, which is −8.4 cm from the isocenter, the geometric distortion was reduced from 5.4 pixel to 1.4 pixel by global shimming, to less than 0.8 pixel by dynamic shimming. Pixel shifts in the anterior part of the brain are larger than those more posterior. The RMS pixel shift in anterior slice 14 (7.2 cm from isocenter) reaches 4.7, but is about 1.9 pixel after dynamic shimming, and 2.5 pixel after global shimming. Images of this slice before and after shimming are shown in Fig. 6B. We discarded the signal variation so that geometric distortion could be estimated directly. Image A shows the undistorted "brain mask" (resized to 64×64) of slice 14. Image B shows the image shape before any shimming. There was clearly an overall image offset along the phase encoding direction (vertical axis) besides other distortions. C and D show the image shape after global shimming and dynamic shimming, respectively. Field maps of this slice can be found in Fig. 5 II. The global shimming corrected the center frequency ($Z0$) but caused large field gradients at the left and right side of the brain. These field gradients expanded the pixels in these two areas and resulted in the distorted image in Fig. 6B(c). After dynamic shimming, the field was more homogeneous at these areas so distortions were reduced.

Note that the RMS pixel shift curve in Fig. 6A looks similar with the standard deviation curve in Fig. 2. This is because the pixel shift is proportional to the field homogeneity (Eq. (7)), and the RMS is an estimate of the standard deviation when the arithmetic mean is near zero. Also note that we introduce the RMS pixel shift as a measure that summarizes the geometric distortion over entire slice. This single value gives a sense of the "typical" geometric distortions in the slice. Although at some slices, the RMS pixel shift after dynamic shimming is only slightly smaller (better) than that of global shimming, considerable improvements may be found in some local areas of this slice. For example at slice 6, which is −2.4 cm from isocenter, RMS pixel shift after dynamic shimming is 1.13, only 0.03 smaller than that of global shimming. However, a maximum 2.69 pixels improvement was observed at some points in this slice.

To demonstrate the effectiveness of higher order dynamic shimming, we compared the field distribution, geometric distortion, and signal intensity after first order dynamic shimming ($Z0$, Z, X, and Y), second order dynamic shimming ($Z0$, Z, X, Y, $Z2$, ZX, ZY, $X2$–$Y2$, and XY), and dynamic shimming with all the available shim terms. Fig. 7 shows the homogeneity (standard deviation) of the field distributions. The average standard deviation was 42.7 Hz after first order dynamic

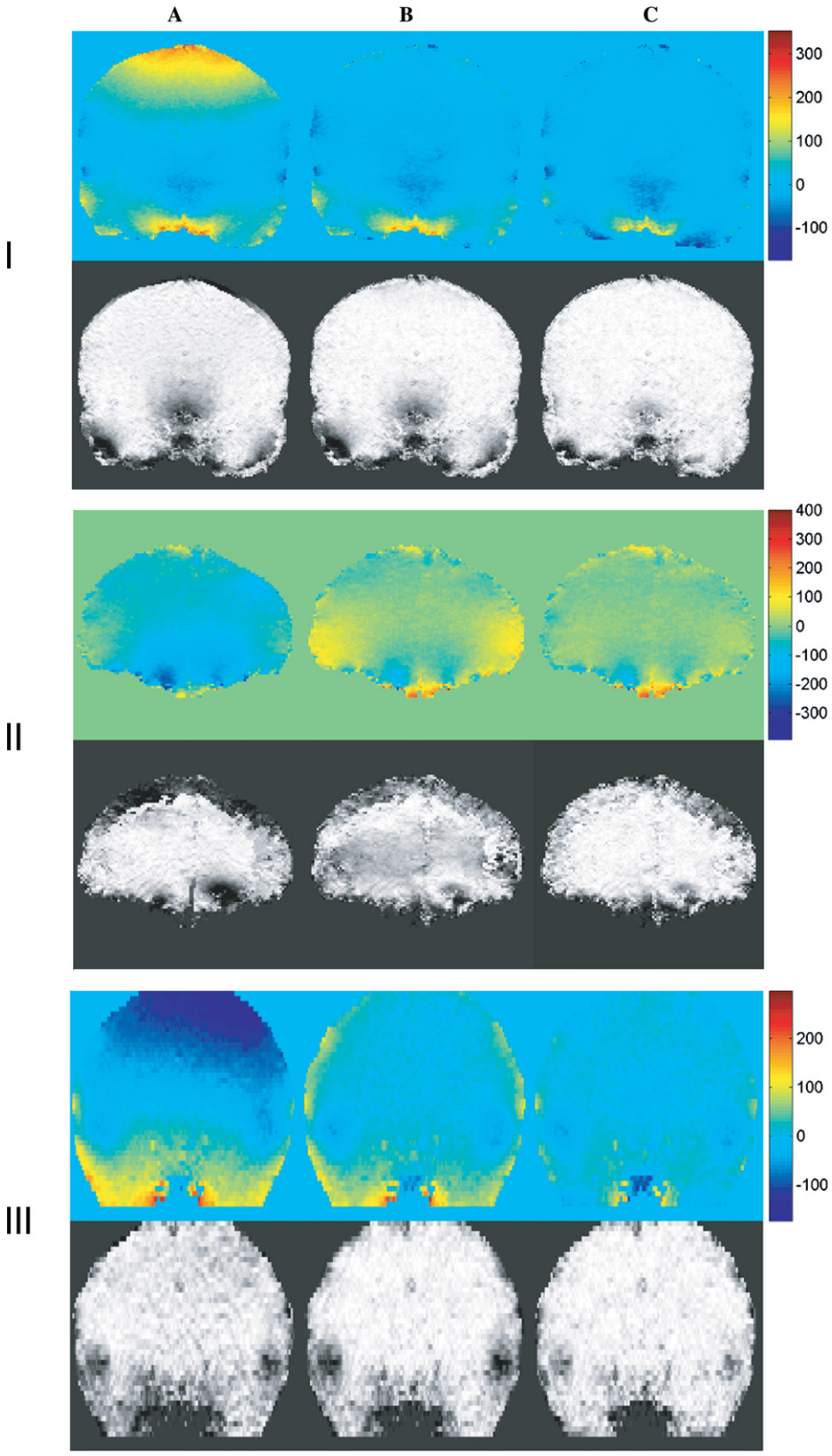

Fig. 5. Simulated field maps and signal intensities of three slices before and after different shimming methods at 7 T. (A) Before shimming; (B) after global shimming; (C) after dynamic shimming. I and II are coronal slices 1.2 and 7.2 cm apart from isocenter, respectively. III is an axial slice 1.8 cm from isocenter. Field maps before shimming were experimentally measured.

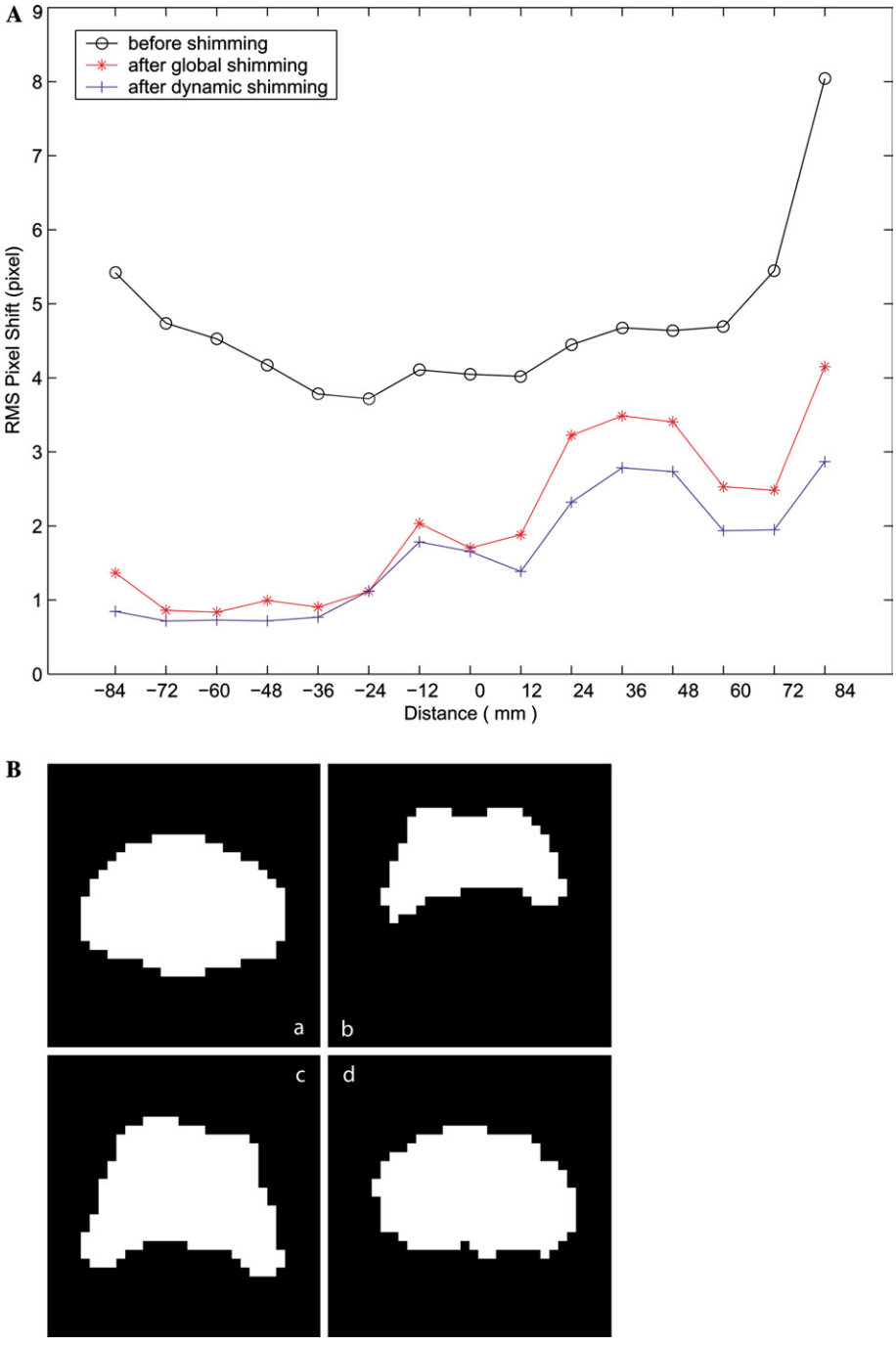

Fig. 6. (A) Simulated RMS pixel shift along phase encoding direction of a typical gradient echo EPI experiment before and after shimming at 7 T with 125 kHz bandwidth, 0.2 ms gradient ramp time and 64×64 matrix size. (B) Simulated geometric distortion of slice 14 (7.2 cm from isocenter) before and after shimming at 7 T. Signal intensity variation not shown. a, original (distortion-free) image; b, before shimming; c, after global shimming; and d, after dynamic shimming.

shimming. It reduced to 28.7 Hz if second order shims were involved and 25.8 Hz if we used all 18 shims. The average standard deviation of field before shimming was 66.3 Hz. Signal intensity improvements are shown in Fig. 8A. and field maps and the signal intensity of slice 9 (1.2 cm from isocenter) are shown in Fig. 8B. The signal intensity improvement was calculated as $(I_d - I_0)/I_0$ in which I_d is the mean signal intensity after dynamic shimming, I_0 is the mean signal intensity before shimming. Compared with first order dynamic shimming, dynamic shimming with second order correction ability only can considerably improve field homogeneity and is often adequate for human brain imaging. Although a full set of 18 shims gives the best performance, the improvement from the 3rd and higher orders is small.

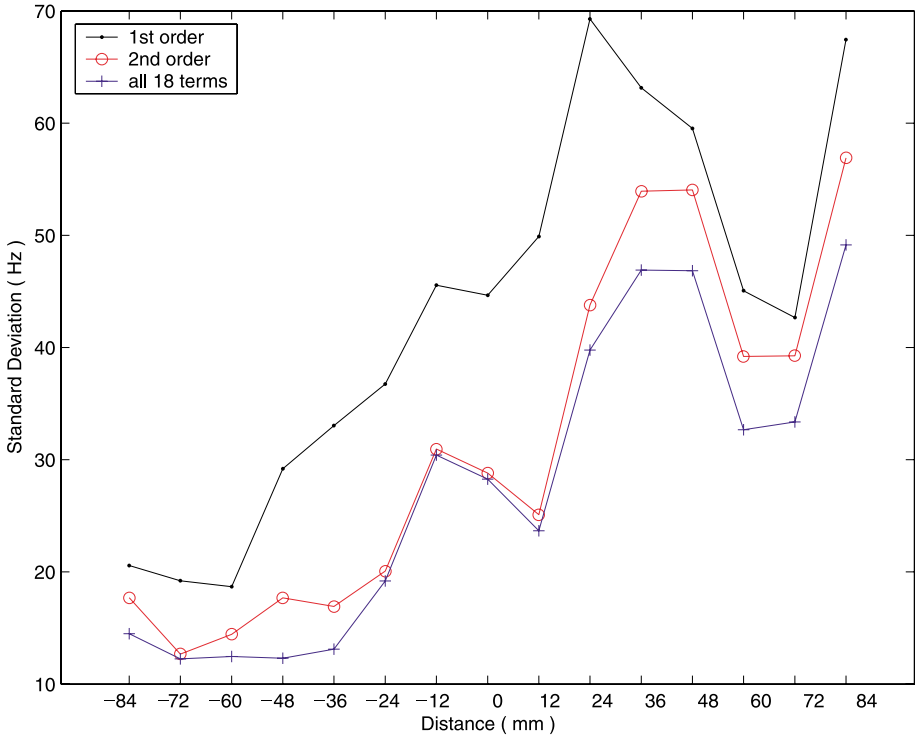

Fig. 7. Comparison of simulated homogeneity (standard deviation) of 15 slice field maps after different order dynamic shimming at 7 T.

The magnetic field distribution within a human brain depends on the geometry and slice orientation. Usually the axial slice has a more homogenous field distribution because of its symmetry with respect to the magnet axis. Peak shim gradients of 2nd order dynamic shimming at different orientations are shown in Table 2. These data were calculated using the 3D coronal field maps. Although shim gradients change when shimming different subjects, these data give an estimate of required shim strengths.

A major potential concern in higher order dynamic shimming is the creation of eddy current effects. In a dynamically shimmed EPI sequence, shim currents must be updated for each slice within the repetition time TR and these shim fields should remain constant throughout slice excitation and readout. The rise time of currents within shim coils can be very short so that shim fields can be switched rapidly. However, such rapid field changes may induce eddy currents in the nearby conductive material and the fields generated by eddy currents decay not so rapidly. If the settling times of shim coils are longer than the time interval between shim updating and RF excitation, eddy current induced fields may arise, and the resultant temporal phase variation may lead to geometric distortion and other artifacts. The effects of eddy currents can be modeled in terms of the rate of change of field, $\partial B/\partial t$

$$\frac{\partial B}{\partial t} = \frac{\text{change in shim gradient} \times l^n}{\text{rise time}}. \quad (15)$$

Here l is the volume dimension over which the shim gradient acts, n is the order of the shim term. From this equation, we can see that eddy current effects will be decreased if the variations in shim gradient between slices is small. Then the settling time would not be a problem for dynamic shimming. de Graaf et. al [9] reported that in their implementation on a small bore system, the settling time of all first and second order shims was less than 10 ms. For human brain shimming, active shielding of higher order shim coils may be required to avoid eddy current effects. Table 1 shows the shim current gradient (in mG/cm^n) of all the first- and second-order shim terms in the 15 slice dynamic shimming and global shimming simulation. Large changes of shim gradient usually occur in regions where large susceptibility artifacts exist. However, the slice imaging order could be changed to obtain smoother shim gradient changes once the required shim gradients have been calculated.

4. Discussion

A major advantage of dynamic shimming over other methods such as Tailored RF, z-shimming and various post-processing methods is its ability to correct both signal loss and geometric distortion. It reduces the sources of susceptibility artifacts before data acquisition. It is also more efficient in use of time compared with z-shimming and multi-reference methods since it does not need

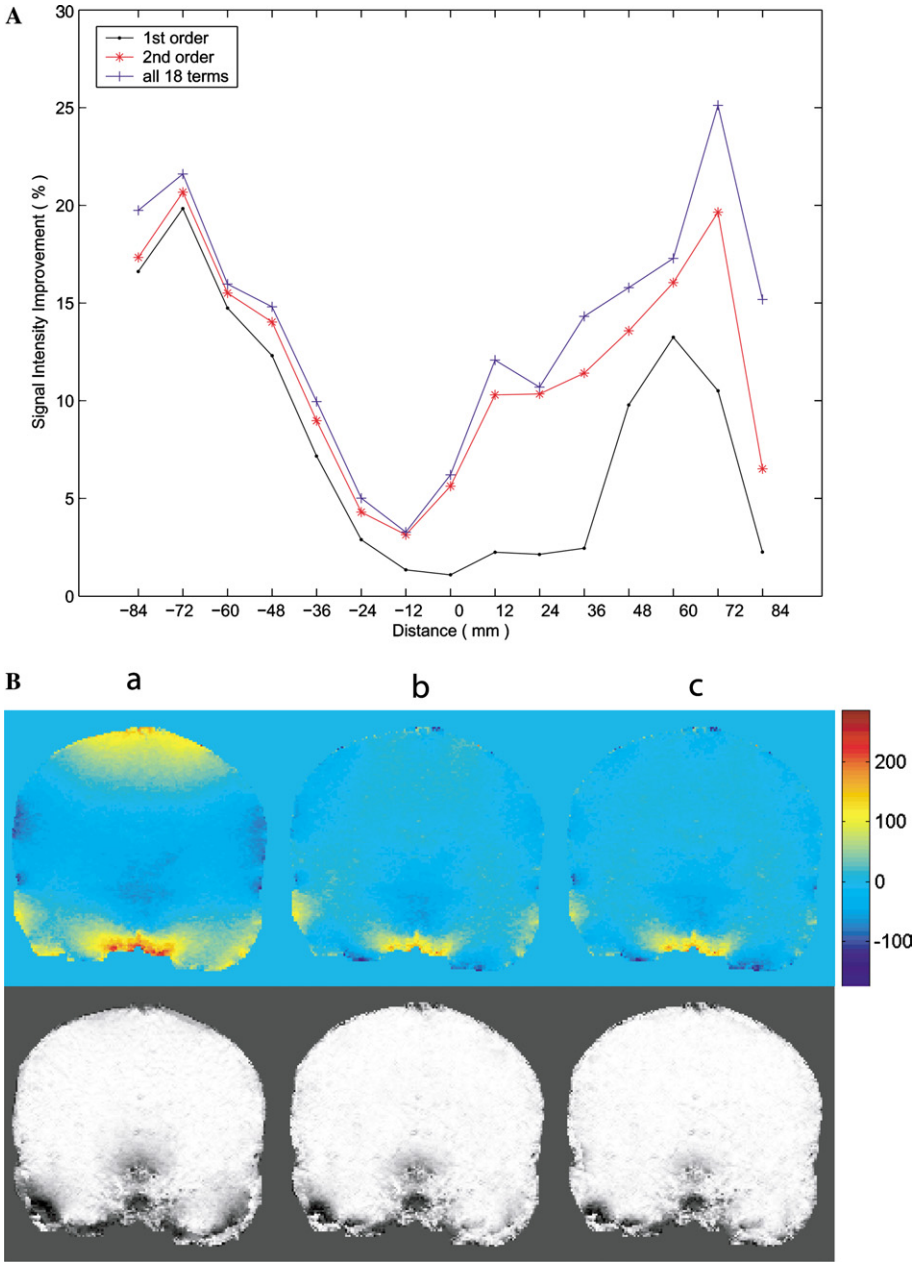

Fig. 8. (A) Comparison of simulated homogeneity (standard deviation) of 15 slice field maps after different order dynamic shimming at 7 T. (B) Simulated field maps and signal intensities of slice 9 (1.2 cm from isocenter) after (a) 1st order dynamic shimming (b) 2nd order dynamic shimming (c) all 18 terms dynamic shimming at 7 T. Field map is in Hz.

Table 2
Simulated shim peak gradients of 2nd order dynamic shimming at 7 T

	Shim peak gradients (mG/cm^n)								
	$Z0$	Z	X	Y	$Z2$	ZX	ZY	$X2–Y2$	XY
Axial	320.38	72.70	10.45	37.67	3.76	0.56	2.51	0.39	0.10
Coronal	168.67	153.84	15.51	43.90	3.41	0.71	6.44	1.17	0.22
Sagittal	85.34	36.98	20.80	8.51	1.05	2.20	0.51	0.22	0.25

n is the order of shim term, $n = 0$ ($Z0$), $n = 1$ (Z, X, Y), and $n = 2$ ($Z2, ZX, ZY, X2–Y2, XY$).

the scan to be repeated several times to obtain a set of images for post-processing. It does however require a field map of the object.

Conventional automatic shimming optimizes the field homogeneity over the whole volume of interest. To further improve the field homogeneity, localized shimming

and/or higher order shimming should be considered. Dynamic shimming is essentially a localized shimming technique. It optimizes the field homogeneity within each slice to be imaged by weighting the shim calculation with the field distribution over that slice at the expense of the field conditions over other slices. Our simulation studies have shown that higher order dynamic shimming is an efficient way to improve field homogeneity in multi-slice MR imaging. It is beneficial for fMRI because of its ability to reduce pixel shifts and signal losses in echo planar imaging. It would also benefit 3D spectroscopic imaging when the main field inhomogeneity within a large field of view often exceeds the chemical-shift difference between water and fat peaks.

In our study, we used three adjacent slices instead of a single slice to compute the field corrections, so that slice-selection shim terms could be determined and signal losses in the slice-selection direction could be recovered. In Blamire et al. [6] and de Graaf et al.'s [9] studies, since the slice thickness is assumed to be infinitely small, only in-plane shim terms could be determined by mapping the field along numbers of linear projections (using FLATNESS [8]). Another experiment is then needed to measure and calculate the (linear) shims along the slice-selection direction.

Field mapping and shim calculations may be implemented as a pre-scan procedure, so they are performed only once for a specific volume of interest. Accurate field mapping is very important for shimming. Although FASTMAP or its "slice-shimming" version, "FLATNESS" can save a lot of time, they are designed for small scale spectroscopic imaging. When applied to large scale brain field mapping, where the field distribution changes rapidly at the borders of different tissues, the accuracy of these approaches is limited, and a more comprehensive method is required. We used gradient echo sequences at different T_E to compute the field. The speed of field mapping with this phase imaging method can be improved. For example, we have recently developed a low resolution "fast asymmetric spin echo" sequence for this purpose. Another advantage of such field mapping methods is that the images are almost "distortion free," making it easier and more accurate for shim calculations than EPI based field mapping [4,18]. If the region of interest is a subset of the FOV, segmentation on the field maps before shim calculations may be used as a further localization/weighting process.

In our simulation, limitations of obtainable shim strengths were not considered. It is likely that, for some regions where higher order field compensation needs large shim currents, current hardware will not be able to meet this demand. Wen and Jaffer [22] have proposed a method that modifies the target function in the optimization that takes account of such shim current constraints. This method can be used in practical dynamic shim calculations.

5. Conclusion

We have presented a computer simulation of higher order multi-slice dynamic shimming at high field. The effectiveness of higher order dynamic shimming is demonstrated by considering the signal intensity and geometric distortions of a typical echo planar imaging experiment. The results of our simulations provide the basic for designing dynamic shimming for use with high field human imaging. To reduce susceptibility artifacts, which are quite severe in temporal and anterior frontal regions of the brain, dynamic shimming with at least second order corrections is necessary.

References

[1] J.F. Schenck, The role of magnetic susceptibility in magnetic resonance imaging: MRI magnetic compatibility of the first and second kinds, Med. Phys. 23 (1996) 815–850.
[2] P. Webb, A. Macovski, Rapid, fully automatic, arbitrary-volume in vivo shimming, Magn. Reson. Med. 20 (1991) 113–122.
[3] E. Schneider, G. Glover, Rapid in vivo proton shimming, Magn. Reson. Med. 18 (1991) 335–347.
[4] T.G. Reese, T.L. Davis, R.M. Weisskoff, Automated shimming at 1.5 T using echo-planar image frequency maps, J. Magn. Reson. Imag. 5 (1995) 739–745.
[5] R. Gruetter, Automatic, localized in vivo adjustment of all first- and second-order shim coils, Magn. Reson. Med. 29 (1993) 804–811.
[6] A.M. Blamire, D.L. Rothman, T. Nixon, Dynamic shim updating: a new approach towards optimized whole brain shimming, Magn. Reson. Med. 36 (1996) 159–165.
[7] G. Morrell, D. Spielman, Dynamic shimming for multi-slice magnetic resonance imaging, Magn. Reson. Med. 38 (1997) 477–483.
[8] J. Shen, D.L. Rothman, H.P. Hetherington, J.W. Pan, Linear projection method for automatic slice shimming, Magn. Reson. Med. 42 (1999) 1082–1088.
[9] R.A. de Graaf, P.B. Brown, S. Mcintyre, D.L. Rothman, T.W. Nixon, Dynamic shim updating (DSU) for multislice signal acquisition, Magn. Reson. Med. 49 (2003) 409–416.
[10] J. Frahm, K.D. Merboldt, W. Hanicke, Direct FLASH MR imaging of magnetic field inhomogeneities by gradient compensation, Magn. Reson. Med. 6 (1988) 474–480.
[11] R.T. Constable, Functional MR imaging using gradient-echo echo-planar imaging in the presence of large static field inhomogeneities, J. Magn. Reson. Imag. 5 (1995) 746–752.
[12] Q.X. Yang, B.J. Dardzinski, S. Li, P.J. Eslinger, M.B. Smith, Multi-gradient echo with susceptibility inhomogeneity compensation (MGESIC): demonstration of fMRI in the olfactory cortex at 3.0 T, Magn. Reson. Med. 37 (1997) 331–335.
[13] G.H. Glover, 3D z-shim method for reduction of susceptibility effects in BOLD fMRI, Magn. Reson. Med. 42 (1999) 290–299.
[14] Z.H. Cho, Y.M. Ro, Reduction of susceptibility artifact in gradient-echo imaging, Magn. Reson. Med. 23 (1992) 193–200.
[15] N. Chen, A.M. Wyrwicz, Removal of intravoxel dephasing artifact in gradient-echo images using a field-map based RF refocusing technique, Magn. Reson. Med. 42 (1999) 807–812.
[16] V.A. Stenger, F.E. Boada, D.C. Noll, Three-dimensional tailored RF pulses for the reduction of susceptibility artifacts in T2*-weighted functional MRI, Magn. Reson. Med. 44 (2000) 525–531.

[17] P. Jezzard, R.S. Balaban, Correction for geometric distortion in echo planar images from B0 field variations, Magn. Reson. Med. 34 (1995) 65–73.
[18] P.J. Reber, E.C. Wong, R.B. Buxton, L.R. Frank, Correction of off resonance-related distortion in echo-planar imaging using EPI-based field maps, Magn. Reson. Med. 39 (1998) 328–330.
[19] N.K. Chen, A.M. Wyrwicz, Optimized distortion correction technique for echo planar imaging, Magn. Reson. Med. 45 (2001) 525–528.
[20] H. Zeng, R.T. Constable, Image distortion correction in EPI: comparison of field mapping with point spread function mapping, Magn. Reson. Med. 48 (2002) 137–146.
[21] F. Romeo, D.I. Hoult, Magnet field profiling: analysis and correcting coil design, Magn. Reson. Med. 1 (1984) 44–65.
[22] H. Wen, F.A. Jaffer, An in vivo automated shimming method taking into account shim current constraints, Magn. Reson. Med. 34 (1995) 898–904.